Measurements of gravity and gravity-capillary waves in horizontal gas-liquid pipe flow using PIV in both phases

Birvalski, M.; Tummers, M. J.; Henkes, R. A W M

DOI
10.1016/j.ijmultiphaseflow.2016.09.003

Publication date
2016

Document Version
Accepted author manuscript

Published in
International Journal of Multiphase Flow

Measurements of gravity and gravity-capillary waves in horizontal gas-liquid pipe flow using PIV in both phases

M. Birvalski[a,*], M.J. Tummers[a], R.A.W.M. Henkes[a,b]

[a]*Laboratory for Aero- & Hydrodynamics, Delft University of Technology, 2628 CA Delft, The Netherlands*
[b]*Shell Projects & Technology, 1030 BA Amsterdam, The Netherlands*

Abstract

An experimental study was performed in stratified wavy flow of air and water through a horizontal pipe. The velocity fields in both phases were measured simultaneously using PIV and the interfacial shape was resolved using a profile capturing technique. The objective of the study was to investigate the interfacial characteristics and the velocities of the liquid and gas phases in two wave patterns: '3D small amplitude' and '2D large amplitude' waves. The wave patterns were shown to consist of gravity and gravity-capillary waves, respectively, with substantial differences in the wave characteristics and liquid velocities. Contrary to this, the effect of the waves on the gas velocities was rather similar in both wave regimes, with both wave regimes causing an increase in the velocity fluctuations close to the interface. The current measurements also produced a valuable dataset that can be used to further improve the numerical modeling of the stratified flow pattern.

Keywords: stratified wavy pipe flow; gravity waves; gravity-capillary waves

1. Introduction

Stratified gas-liquid flow through pipes occurs in many branches of industry. In some applications, e.g. in the natural gas industry, stratified flow is the dominating flow pattern, since gas-condensate pipelines typically operate at low liquid loading conditions. In particular, stratified *wavy* flow is prevalent since the gas velocities are typically high enough to produce waves. The continuing experimental research focused on this flow pattern aims to elucidate the complex two-phase flow phenomena, such that more accurate models can be constructed for use in practical applications.

The stratified wavy region is empirically divided into several wave patterns. Here, the categorisation proposed in Birvalski et al. (2015) is followed (similar to Espedal, 1998; Fernandino & Ytrehus, 2006), which corresponds to the wave patterns observed in a relatively small diameter pipe ($D = 5$ cm) using air and water at atmospheric conditions. It distinguishes four wave patterns: 2D small amplitude (SA), 3D small amplitude, 2D large amplitude (LA) and 3D large amplitude waves. In our previous studies (Birvalski et al., 2014, 2015), the 2D SA and 3D SA wave patterns were investigated. It was shown that the 2D SA regime, with rather uniform waves of approximately 12-14 mm length and less than 2 mm height, corresponds to the capillary-gravity regime, as predicted by linear wave theory (e.g. Dean & Dalrymple, 1998). The 3D SA wave regime, on the other hand, with a less uniform wave pattern, and waves of 22-24 mm length and similar height corresponds to the gravity-capillary regime. Both wave patterns were shown to have a celerity close to the minimum celerity predicted by linear wave theory (i.e. $\sim$0.23 m/s), and velocity profiles that correspond to linear theory predictions close to the wall and in the bulk, while these deviate close to the interface due to wave asymmetry. The interaction between the waves and the bulk flow was also studied (Birvalski et al.,

*Corresponding author
Email address: m.birvalski@academy.marin.nl (M. Birvalski)

2015). It was found that the transition from 2D SA to 3D SA waves is caused by the laminar-to-turbulent transition of the liquid layer. The other two wave patterns - 2D LA and 3D LA - were observed to have a substantially longer wave length (2-3 times greater than in SA regimes) and a height typically larger than 2 mm, consistent with the observations that were reported by Andritsos & Hanratty (1987); Strand (1993); Espedal (1998). The two regimes, however, differ in that the 2D LA pattern is rather uniform, while the 3D LA pattern (also called 'roll waves' or 'Kelvin-Helmholtz waves') is highly non-uniform, with large interfacial disturbances suddenly appearing and moving quickly along the interface.

The present study is a continuation of our investigation of the stratified gas-liquid flow regime (see Birvalski et al., 2014, 2015). The first objective of the present study is to obtain detailed wave statistics for cases in the 3D SA and the 2D LA regime, including the transition from one wave regime to the other. This will provide insight into the dominant forces acting on the interface, producing the observed wave patterns. The second objective is to study the influence of the 3D SA and the 2D LA wave patterns on the gas and liquid velocities, which will lead to more understanding of integral flow quantities (such as bulk velocity, holdup or pressure drop) that are relevant in engineering practice.

One of the first to measure velocities in the gas phase of two-phase pipe flow were Andreussi & Persen (1987), Strand (1993), Dykhno et al. (1994) and Paras et al. (1998), while the liquid velocities were measured by Paras & Karabelas (1992) and Strand (1993). All these studies used single-point measurement techniques, either intrusive (Pitot tube, HWA) or non-intrusive (LDA). It has been observed that pipe flow in most aspects resembles channel flow, although some differences were also noted. For example, at certain flow conditions, pipe flow may have a different wave amplitude distribution in the spanwise direction, which produces a change in the secondary flow direction when compared to channel flows (Flores et al., 1995). More recently, flow measurement techniques for two-phase pipe flows were improved by using a non-intrusive planar velocity measurement technique (PIV), which provided more details of the velocity fields. Specifically, it opened the trough-to-crest region for investigation (if the interfacial profile was resolved), and enabled the measurement of statistical quantities based on spatial derivatives of the velocity (such as vorticity or swirl) in flow analysis. The first to apply PIV in gas-liquid pipe flow were Vestøl & Melaaen (2007). Recently, Ayati et al. (2014) also applied PIV in both phases of the flow, and resolved the air-water interface. Both studies are, however, of limited scope and reported difficulties in obtaining measurements in some parts of the flow due to light reflections on the interface or the pipe wall.

In Birvalski et al. (2014), PIV in conjunction with profile capturing was successfully employed to resolve the profile shape and the velocities in the *liquid* phase from the wall to the wavy interface. Here, we extend our measurements to include also the gas phase. By studying the velocities in both phases, i.e. in the entire pipe cross-section along the centre plane of the pipe, the mechanisms governing the two-phase flow are further elucidated. Besides the physical insights gained through these measurements, also a valuable database has been created which can be used to improve the accuracy of stratified flow models and, consequently, of two-phase flow simulations.

2. Experimental set-up

The flowloop used in the present study is described in detail in Birvalski et al. (2014). It is a horizontal pipe of $D = 5$ cm inner diameter made of PMMA and glass (for the test section), with a total length of 10 m or 200D. Air and water at atmospheric conditions enter the pipe through a Y-shaped inlet, and discharge freely into an open container. Air is driven by a fan and its flowrate is measured using a turbine flow meter. Water is circulated using a pump and its flowrate is measured using a Coriolis flow meter. The glass test section is positioned 7.5 m ($150D$) from the inlet.

In comparison to our previous study, the optical measurement system is extended with a second PIV system, which is used to measure the gas phase velocity (see figure 1a). The camera configuration consists of 1) a water-side PIV camera (PCO Sensicam, CCD with 1280×1024 pixels, 12-bit, equipped with a Nikon Mikro-Nikkor 60 mm f/2.8D lens) pointing 16.2° upwards, looking through a water-filled view-correction box into the liquid phase, 2) a Profile camera (PCO Sensicam qe, CCD with 1376×1040 pixels, 12-bit, with a Nikon Mikro-Nikkor 60 mm f/2.8D lens), pointing 15.8° downwards, recording the position of the interface and 3) an air-side PIV camera (PCO.2000, CCD with 2048×2048 pixels, 14-bit, equipped with a

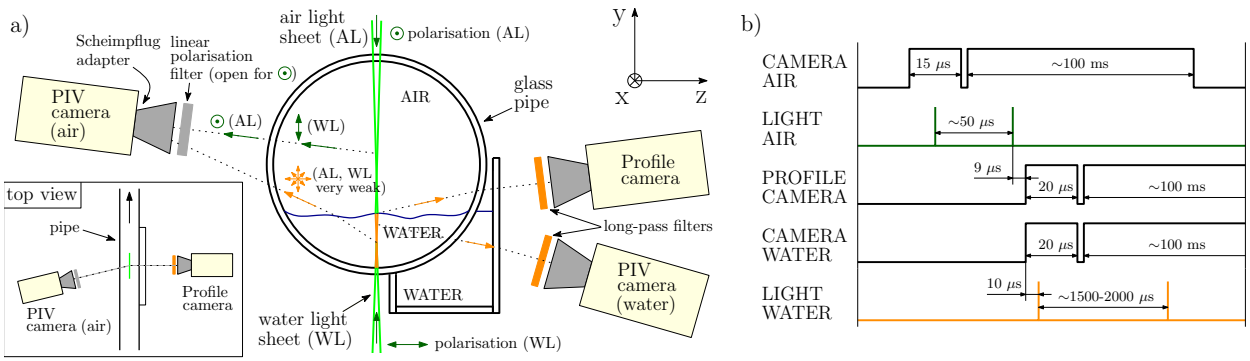

Figure 1: Schematic view of the test section (a) and the timing diagram (b). The final time separation between the instantaneous air and water velocity measurements is $O(1)$ ms.

Nikon Mikro-Nikkor 55 mm f/2.8D lens), pointing 14.3° downwards and tilted ~ 20° in the horizontal plane, looking downstream at the gas phase. The fields of view (FOV) of the cameras are ~50×40 mm^2 (water PIV), ~58×44 mm^2 (profile) and ~54×54 mm^2 (air PIV).

The seeding particles in the flow are illuminated by two double-pulsed Nd:YAG lasers (emitting light at 532 nm). A Continuum Minilite used in low power mode (~1.2 mJ/pulse) fires from below the test section into the liquid at 2 Hz, while a Litron Nano L 50-50 fires from above into the gas at the same pulse rate, emitting approximately 22 mJ/pulse. The liquid is seeded with fluorescent particles from a commercially available acrylic paint (Lefranc & Bourgeois, Fluorescent Light Orange, particle size ~5-20 μm). The fluorescent particles, in combination with long-pass optical filters (Hoya O56) fitted to the water-side PIV and profile cameras, are used to eliminate light reflections originating from the pipe wall and the interface. A water based (and therefore water-soluble) liquid was used to generate droplets for air seeding. The use of water-soluble liquid ensured that no film (which could change the interfacial dynamics) was formed on the interface.

The light coming from the two lasers is transformed into overlapping vertical sheets (~70 mm wide) belonging to the pipe axis. If we were to measure in both phases at the same time, the light coming from e.g. the water laser would reach the air PIV camera and vice-versa, i.e. there would be cross-talk between the two PIV systems. This problem arises because the double-frame cameras used for PIV do not have the capability to control the exposure of the second frame; the exposure remains fixed at ~100 ms, i.e. the time needed to transfer the first frame to memory. To avoid cross-talk between the two PIV systems, the following measures were taken. First, the polarization of the water laser light was changed from horizontal to vertical by altering the light path using two mirrors. With the laser head placed horizontally (and emitting a horizontally polarized beam), pointing perpendicularly to the pipe, one mirror was placed in front such that it reflected the light in the horizontal plane. The second mirror is placed in the light path of this beam and it reflected the light upwards. The light coming from the water laser was thus vertically polarized ('vertical' in reference to the light scattered horizontally by the particles or droplets, see figure 1a). The air laser was horizontally polarized, which means the two lasers were polarized in perpendicular directions. In this way, the water laser light scattered by the air seeding droplets could be filtered by placing a horizontally oriented linear polarization filter in front of the air PIV camera. On the other hand, the fluorescence emitted by the seeding particles in the liquid that are illuminated by the air laser is randomly polarized, so it is not fully filtered by the linear filter. Despite this, no further filtering was necessary, since the intensity of fluorescent light that reaches the air PIV camera is very weak, i.e. it is below the noise level of the camera. This light is only a fraction of the intensity of the original water laser light (which is itself approximately 20 times weaker than the air laser light), and it is further partly removed by the linear polarizer, which transmits only approximately 25% of the randomly polarized light. This configuration prevented the contamination of the air PIV frames with light from the water laser. To prevent the light from the air laser reaching the water PIV and profile cameras, the air laser was timed to fire just before the exposure of the first water PIV

and profile frames starts (see figure 1b).

The final time separation of air and water PIV vectors is approximately 1 ms. Since the liquid phase remains essentially frozen in this time span, the final result approximates the instantaneous vector fields at the time of the air flow measurement.

The calibration of the cameras was performed using a grid of 0.5 mm diameter dots, spaced 1 mm apart, printed on an overhead sheet and placed in the plane of the laser light sheets. The grid was fixed to a brass plate, that could be rotated over 180° around the pipe axis after a calibration image was taken by the air PIV camera, so that calibration images can be taken with the water PIV and profile cameras as well. The mapping function from camera to real-world coordinates was determined using LaVision's DaVis 8 software, which was also used for velocity field calculation.

Further details of the experimental technique are found in Birvalski (2015).

3. Data reduction and processing

For every measurement case, 2020 double-frame images were collected by each of the three cameras. The images collected by the profile camera are used first in a profile detection procedure to determine the interface shape in both frames of every image. The interfacial profile was detected using an edge-detection algorithm, in a similar way as in e.g. Mukto et al. (2007) and Siddiqui & Loewen (2007). Details of the profile detection procedure are reported in Birvalski (2015). The obtained profiles were cross-correlated in the horizontal direction resulting in the profile displacement, which was then divided by the pulse time separation to arrive at the profile velocity, v_p. The interface detected in the first frame of every image was displaced downstream by half of the detected displacement and subsequently used to produce a vector mask for the PIV results.

Both the air-side and the water-side PIV images were processed using a multi-pass, multi-grid adaptive cross-correlation procedure implemented in LaVision's DaVis 8 software. The final interrogation window size for PIV in air was 16×16 pixels and for PIV in water 8×8 pixels. In both cases, the interrogation windows were overlapping by 50%. The resulting vector grid spacing was ∼0.19 mm for air and ∼0.16 mm for water. The final vector results were obtained by first replacing the outliers (detected by standard techniques such as local median filter, correlation peak ratio threshold, etc.) with higher-order correlation peaks or interpolation, followed by applying a 3×3 vector smoothing filter.

For some cases considered in the present study, phase averaging was performed to decompose the velocity field into the time-averaged, the wave-induced and the fluctuating velocity component (see e.g. Hussain & Reynolds, 1970). The wave phase was detected using an algorithm initially proposed by Siddiqui & Loewen (2010). It works by identifying 'wave quarters' in the instantaneous interfacial profiles resulting from the profile detection technique. These quantities were then used to calculate wave statistics such as wavelength λ, wave height H, crest/trough steepness, etc. Due to the finite FOV width, the technique is limited in terms of the maximum wavelength that it can fully resolve (i.e. adequately represent in a statistical sense). Theoretically, quarters belonging to a monochromatic, sinusoidal, wave field with a wavelength up to twice the FOV width (FOV_W) can be fully resolved (see Birvalski et al., 2014), which corresponds to waves with $\lambda \leq 100$ mm, given the FOV_W of 50 mm. A wave field with $\lambda > 4FOV_W$ ($\lambda > 200$ mm) cannot be resolved at all, since the quarters of such waves are always longer than the FOV_W. As the wavelength increases from 100 mm to 200 mm, the probability of detecting a quarter decreases according to:

$$P_q = \frac{1}{q_L/FOV_W} - 1 \text{ for } 0.5 \leq q_L/FOV_W \leq 1, \tag{1}$$

where q_L is the length of a quarter, i.e. $q_L = \lambda/4$. For example, a wave field with $\lambda = 133.3$ mm ($q_L/FOV_W = 2/3$) has a detection probability of $P_q = 0.5$. This means that for every quarter detected, there is (on average) another one that is missed. The missing quarters are compensated for when calculating the wave statistics by using the weighting factor $m_q = 1/P_q$. In the current example, $m_q = 2$, so every detected quarter of this wavelength would be included in the statistics as if it were detected twice.

Once the phase is determined for all the quarters of a given case, phase averaging of any quantity (velocity, vorticity, etc.) is performed by extracting the values along a wall-normal line at a desired phase

and averaging them using an appropriate coordinate system. In this study, both Eulerian and adaptive coordinate systems are used. The Eulerian coordinate systems in air and water have their origin at the top and the bottom wall, respectively, with the x-axis pointing downstream and the y-axis pointing towards the pipe centre. An intermittency factor is calculated in the trough-to-crest region, since a point in that region is sometimes located in the water and sometimes in the air. An adaptive coordinate system, on the other hand, has an origin on the pipe wall, and an end point fixed to the interface, while the region in between is divided into a certain number of segments of equal length (typically between 50 and 100). Therefore, the height is scaled with the instantaneous height occupied by the given phase, which makes the use of this system particularly beneficial for studying the trough-to-crest region. More details can be found in Birvalski et al. (2014).

4. Results

4.1. Visual observations

Measurements were performed for 21 cases (see figure 2), along lines of constant superficial water velocity (L1-L6), beginning with cases belonging to the 3D SA wave region (cases **101**-**123**) and ending in the 2D LA wave region (cases **131**-**154**); the flow conditions (u_{SL} and u_{SG}) and the measured integral flow quantities (u_L, u_G, h_L and $\Delta p/\Delta x$) for the present cases are reported in Appendix A. Figure 3a shows that the 3D SA wave pattern consists of relatively short and low amplitude waves, and the pattern appears quite irregular. The wave amplitude in the spanwise direction can vary greatly and is typically asymmetrical about the stream-wise vertical plane (hence the name '3D'). These waves were shown (Birvalski et al., 2015) to correspond to the gravity-capillary part of the dispersion relation curve as predicted by linear wave theory. The 2D LA wave pattern consists of longer and higher waves, and the pattern is more regular in comparison to the 3D SA wave pattern (see figure 3b). Their length (shown later to be approx. 5 cm) suggests these can be classified as gravity waves, since the capillary forces have a relatively low influence on the wave propagation velocity at this wavelength. Their amplitude distribution in the spanwise direction is not uniform but decreases from the walls to the pipe centre. However, the 2D LA waves are more symmetric about the stream-wise vertical plane when compared to the 3D SA waves. Close to the walls, the waves have a profile with relatively steep crests and long troughs. Towards the centre, however, the profile is more symmetric and the amplitude of the crests is lower.

The boundary between the two wave patterns in figure 2 was determined visually and represents the position where one type of waves (gravity-capillary or gravity) becomes dominant over the other. It was observed that neither the 3D SA nor the 2D LA regions consist solely of waves of one wave pattern, but of both. If, for example, the liquid flowrate increases, the conditions become more favourable for the occurrence of gravity waves as opposed to gravity-capillary waves. As a result, the 2D LA waves become the dominant wave-type in that region. This is unlike what is observed when going from e.g. 2D SA to 3D SA, or from 2D LA to 3D LA waves. In these regions of the flowmap, a liquid or gas flowrate exists above or below which waves that are characteristic of the other wave pattern do not occur.

4.2. Wave characteristics

As described in Section 3, the phase averaging procedure works by first identifying the wave quarters in the instantaneous interfacial profiles for a given case. When the height and the length of all the quarters are known, these data are processed to arrive at the wave height H, wavelength λ, and wave steepness H/λ for all cases along L1-L6. The results of this procedure are presented in figure 4. The data form two groups: one that includes cases along L1-L3, corresponding to the observed 3D SA region, and the other one along L4-L6, corresponding to the 2D LA region. The values of H and λ of 3D SA waves do not differ much between lines L1-L3 as the value of u_{SG} is increased. In contrast, both the length and the height of 2D LA waves change with increasing values of u_{SL}. For these waves, the increase in u_{SL} results in at least as much change in H and λ as the increase in u_{SG}. Furthermore, the variations in the flowrates do not influence the wave steepness H/λ of 2D LA waves, which remains at a value of $H/\lambda \sim 0.04$ for all values of u_{SG} and u_{SL}.

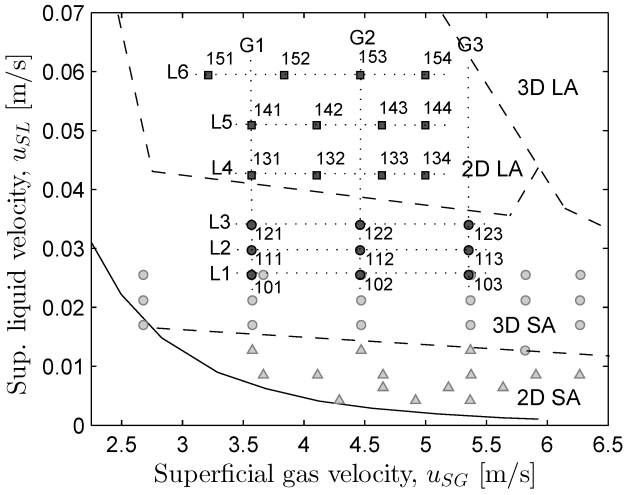

Figure 2: Experimental flowmap. The cases considered in the present study are marked with black symbols and those from our previous study (Birvalski et al., 2015) with gray symbols. The boundaries between the different wave regions are marked with dashed lines, while the solid line marks the boundary between the smooth and the wavy regions. Dotted lines G1-G3 and L1-L6 are used for reference throughout this study. Cases **151**, **132**, **142**, **134**, **144** and **154** are presented alongside cases belonging to G1-G3, since their gas velocity is close to that of lines G1-G3.

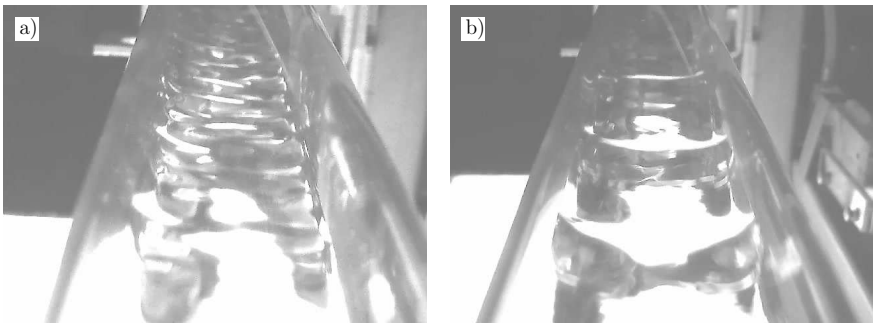

Figure 3: Photographs of the: a) 3D SA and the b) 2D LA wave regimes.

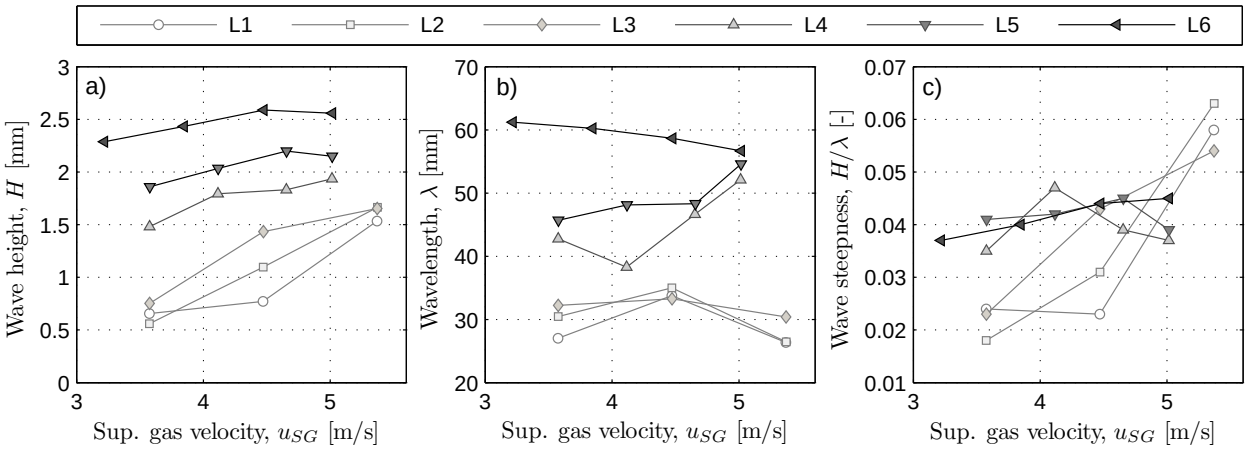

Figure 4: Measured values of the average: a) wave height H, b) wave length λ and c) wave steepness H/λ for cases along lines L1-L6.

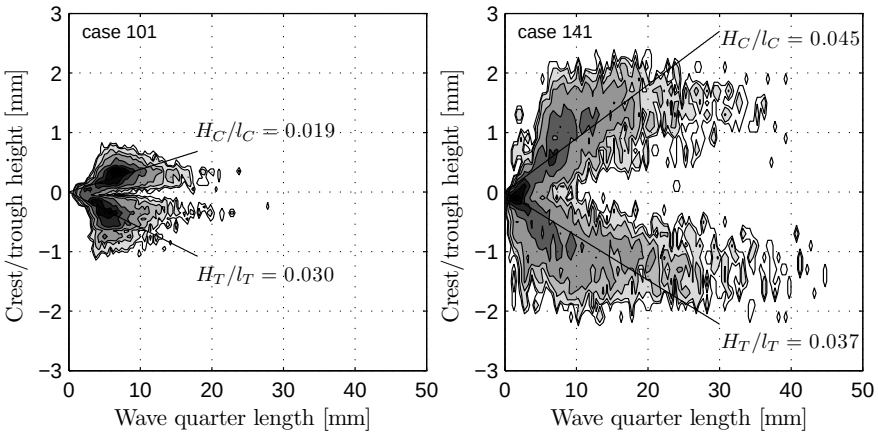

Figure 5: Joint probability distribution of quarter length and height [%]. The plot area was divided into slots with dimensions (W×H) 0.4×0.1 mm^2 for case **101** and 0.5×0.2 mm^2 for case **141** and the probability of encountering a quarter calculated for each slot. The scale for both graphs is 0-2 % (white to black). The steepness of the quarters is shown with solid lines and the values of the crest and the trough steepness are indicated. In case **141**, there is a number of quarters that are longer than $q_L/FOV_W = 0.5$ (25 mm in the present study), which means a correction (eq. 1) is used to arrive at the averaged values for height and length.

The wave steepness is investigated in more detail by determining the joint probability density function (PDF) of quarter length and height. This was done by dividing the full range of quarter heights and lengths into slots and calculating the probability of detecting a quarter in each slot. The joint PDFs for cases **101** (3D SA) and **141** (2D LA) are presented in figure 5. Both cases have quarters with a wide range of heights and lengths. Although PDFs for both cases are fairly symmetrical around the mean liquid level, a difference can still be observed in the steepness of crests and troughs (solid lines in figure 5). For case **101**, the trough is slightly steeper than the crest, and vice-versa for case **141**. This is a confirmation (along with a factor of 2 greater length of case **141** compared to case **101**, see figure 4) that the 2D LA wave pattern is composed of gravity waves.

The details of the wave profile are studied next by combining the average quarter lengths and heights to determine several relative measures of various parts of the wave profile. Figures 6a and 6b show the relative crest length l_C/l_T and the relative crest height H_C/H_T, respectively. A sinusoidal wave has a value of 1 for both of these quantities. For a capillary wave the value of l_C/l_T is larger than 1, and H_C/H_T is less than 1. The opposite is true for a gravity wave. The present measurements of the 3D SA wave pattern (gravity-capillary, L1-L3) show that their profile has the characteristics of a capillary wave, although the asymmetry is much smaller (i.e. closer to sinusoidal) than found in the capillary-gravity (2D SA) waves that were measured previously (Birvalski et al., 2014) which have values of $l_C/l_T \sim 1.25$ and $H_C/H_T \sim 0.64$. It appears that although these waves are classified as gravity-capillary according to their wavelength and the dispersion relation of linear waves, the capillary effects still play a significant role in determining the wave profile and, accordingly, the wave-induced velocities (see later, Section 4.3). The capillary effects appear to persist into the 2D LA wave region (L4-L6), although here a marked change towards a profile shape characteristic of gravity waves is measured. For example, at lower values of u_{SG}, there are cases at all values of u_{SL} (L4-L6) that have a $H_C/H_T > 1$, i.e. the crest larger than the trough, which is a characteristic of gravity waves. However, only several of these also have $l_C/l_T < 1$, whereas one would expect all of them to have $l_C/l_T < 1$. Nevertheless, the measurements show a shift to a gravity wave profile with increasing u_{SL}, as has also been observed visually (see Section 4.1).

Figure 6c shows the relative windward side length l_W/l_L. As expected, all the cases have $l_W/l_L > 1$, which means that the profiles are 'leaning' forward, in the direction of wave propagation. This was also observed previously also in 2D SA waves (Birvalski et al., 2014), and interpreted to be a consequence of the shear between the liquid and the wall. This effect is larger in 2D LA than in 3D SA waves, because 2D LA

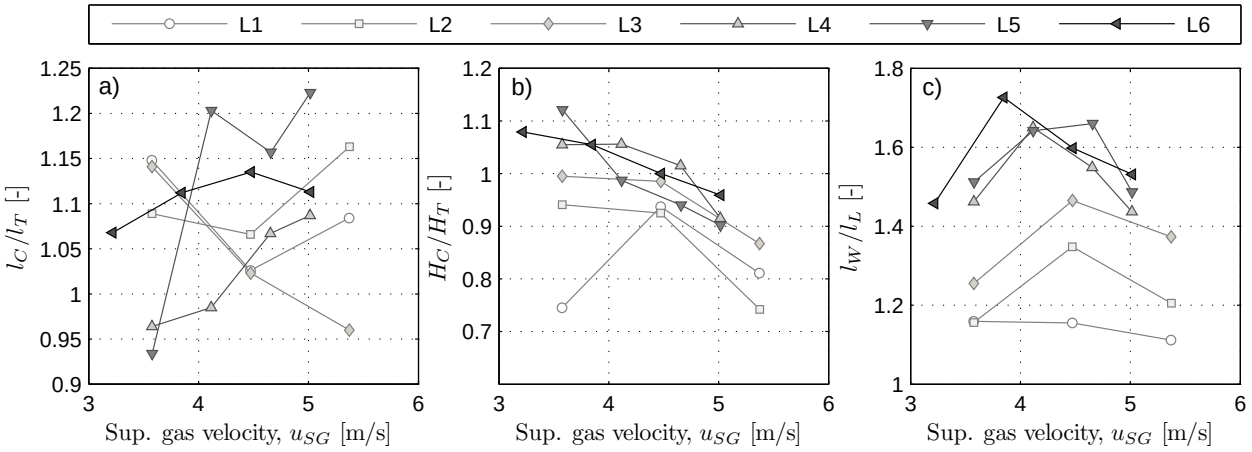

Figure 6: Relative dimensions of different parts of the waves for cases along lines L1-L6: a) relative crest length, b) relative crest height and c) relative windward slope length.

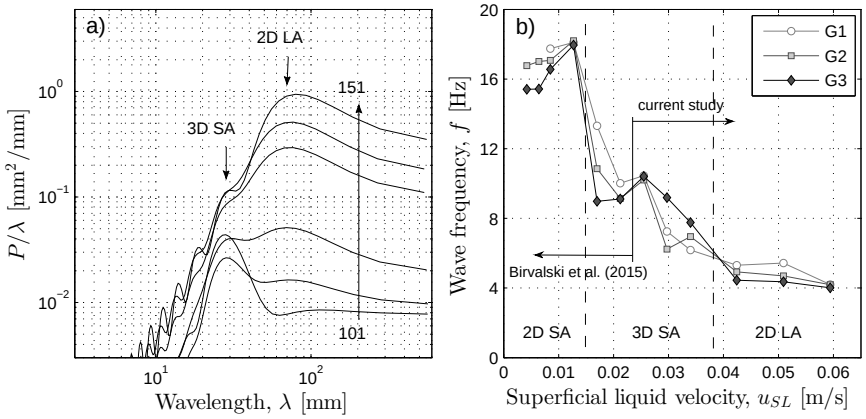

Figure 7: Power spectral density (PSD) for cases along G1 (a) and wave frequency f for cases along G1-G3 (b). Graph b) contains also the 2D SA cases measured in our previous study (Birvalski et al., 2015).

waves have larger wave-induced velocities and therefore also larger wave-induced wall shear stresses.

In Section 4.1, it was reported that waves typical of both the 3D SA and the 2D LA wave patterns occur simultaneously in both regions and that the transition from one pattern to the other is a result of one wave type becoming more frequent than the other. This is further illustrated in figure 7a, where spatial power spectral density (PSD) of the wave profiles is shown for cases **101-151** (along G1). To calculate the PSD, the mean liquid level h_L was first subtracted from the instantaneous interfacial profiles for a given case. The PSD was subsequently calculated for all the instantaneous profiles. Finally, the resulting spectral densities were averaged. Figure 7 indicates that (in accordance with the observations) there appear to be strong contributions to the PSDs at two distinct wavelengths which are indicated by arrows. As one moves from case **101** to case **151** the power of the 3D SA component decreases, while the power of the 2D LA component increases. The change from 3D SA to 2D LA dominance occurs approximately between cases **121** and **131**.

The occurrence of two peaks in the power spectra of wave profiles in stratified flow has been observed previously (see e.g. Strand, 1993; Fernandino & Ytrehus, 2006; Sanchis et al., 2011; Ayati et al., 2015). Strand (1993) and Fernandino & Ytrehus (2006) have reported a flow pattern with peaks at two frequencies that correspond to wavelengths of 2-4 cm and 5-8 cm, in agreement with the results of the present study.

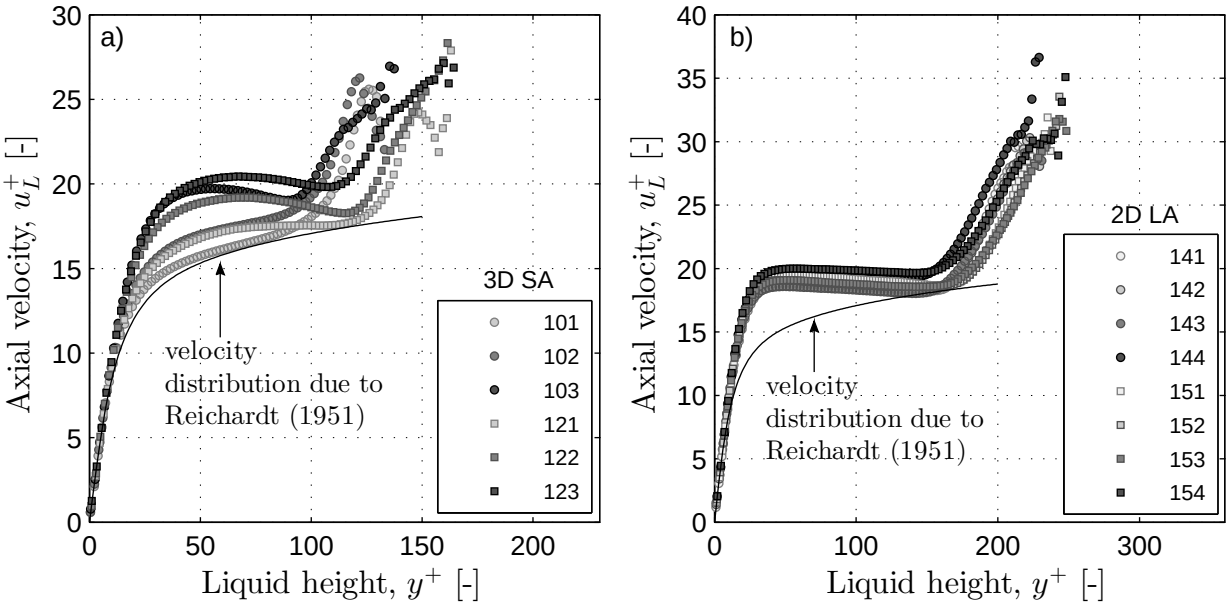

Figure 8: Measured mean axial liquid velocity profiles for cases along lines a) L1 and L3 (3D SA regime) and b) L5 and L6 (2D LA regime), scaled with the measured friction velocity u_τ. The velocity distribution by Reichardt (1951) $u_L^+ = \frac{1}{\kappa}\ln\left(1+\kappa y^+\right) + \frac{B\kappa-\ln\kappa}{\kappa}\left(1-\exp\frac{-y^+}{11} - \frac{y^+}{11}\exp -0.33y^+\right)$ with $\kappa = 0.4$, $B = 5.5$ and $y^+ = \frac{yu_\tau}{\nu}$ is shown for comparison.

In both studies, the two-frequency wave pattern exists as a transitional region between the regions with shorter (2-4 cm) and longer (5-8 cm) waves. Strand (1993) and Sanchis et al. (2011) have also reported on measurements with two frequencies, but corresponding to longer wavelengths that occur at high liquid flowrates, close to the slug flow transition boundary. Furthermore, our previous study (Birvalski et al., 2015) has reported on the relatively sudden change from the short 2D SA waves (12-14 mm) to the longer 3D SA waves (22-26 mm) that corresponds well with the mechanism (described in e.g. (Janssen, 1986; Bontozoglou & Hanratty, 1990)) of period-doubling ($2 \rightarrow 1$) bifurcation, where the second harmonic (with $\lambda \sim 12.1$ mm and $f \sim 16$ Hz in air-water flows) resonates with the fundamental (with $\lambda \sim 24.2$ mm, and $f \sim 8$ Hz), thereby transferring energy and producing the longer wave. It appears that the change of wave patterns in stratified pipe flow occurs at least partly in a stepwise manner, i.e. in relatively sudden changes of wavelength (and frequency) from one wave pattern to the other. To illustrate this, the wave frequency f measured in this and in our previous study (Birvalski et al., 2015), determined as $f = c/\lambda$ (where c is the wave celerity, obtained by subtracting the liquid bulk flow velocity u_L from the profile velocity v_p), along lines G1-G3 is shown in figure 7. As mentioned above, the change of frequency from 2D SA to 3D SA waves corresponds well with the period-doubling mechanism, with f effectively halving (i.e. the period is doubling) from 16-18 Hz to 8-10 Hz. Furthermore, it appears that the change from 3D SA to 2D LA waves involves another frequency halving, from 8-10 Hz to 4-5 Hz. This is supported also by the wave frequencies obtained in a recent study by Ayati et al. (2015).

4.3. Liquid velocities

The velocity fields determined from the PIV measurements are processed to arrive at the time-averaged mean and fluctuating velocities shown in figures 8-12. This was done by extracting instantaneous velocity profiles in the radial direction at 5 axial locations equally spaced within the FOV and averaging them using an Eulerian coordinate system with its origin at the pipe wall.

The profiles of the mean axial velocity (figure 8) for cases along lines L1 and L3 (in the 3D SA regime) and along L5 and L6 (in the 2D LA regime) are scaled with the liquid friction velocity u_τ, where the values

of u_τ were found by fitting a straight line through 3-5 points of the mean velocity profile that are nearest to the wall, in the viscous sublayer. For comparison, the velocity distribution by Reichardt (1951) with constants $\kappa = 0.4$ and $B = 5.5$ is also shown as a solid line. The velocity profiles for the 3D SA cases are linear near the wall (in the laminar sublayer) and transitions into the classical log-law at larger values of y^+ (where $y^+ = \frac{yu_\tau}{\nu}$). Cases with a relatively low wave height (**101**, **102** and **121**) are seen to follow the log-law closely (albeit with a varying constant B) and to have a logarithmic profile shape throughout the bulk of the liquid, i.e. well beyond the buffer layer. Cases with higher waves (**103**, **122** and **123**) still have a logarithmic shape in approximately half of the layer height. However, the mean velocity profile deviates close to the interface, where it has a negative gradient (in accordance with Fabre et al., 1987; Strand, 1993; Fernandino & Ytrehus, 2008).

The effect of the waves is even more pronounced in the 2D LA regime (figure 8b). All the cases deviate strongly from the log-law at all heights at which the log-law is valid. The nearly flat profile in the bulk of the liquid (also with a slight negative gradient) indicates a strong mixing of momentum caused by the relatively high and long waves (compared to those in 3D SA cases) in a relatively shallow liquid layer. It is also observed that the axial velocity profiles scale well with u_τ, which indicates that the waves have a strong influence on the resulting wall shear stress, unlike in the 3D LA cases where u_τ appears to be also significantly influenced by the bulk flow.

Figure 9 shows the wave-induced velocity obtained by subtracting the time-averaged velocity from the phase-averaged velocity. This was done for the cases along lines L2 and L6 at wave phases $\varphi = 0°$ (crest) and $\varphi = 180°$ (trough). In the same figure, the velocity profiles predicted by linear wave theory are shown for comparison. The 3D SA cases have an axial velocity that follows the linear wave predictions closely in the bulk of the layer, with (absolute) values approximately the same at both phases. A deviation from the linear solution is observed close to the interface due to the asymmetry of the wave profiles, which are influenced more strongly by the capillary than the gravity force, as discussed in Section 4.2. Since 3D SA waves have troughs steeper than the crests (see figure 6), the wave-induced velocity close to the interface is higher at $\varphi = 180°$ than at $\varphi = 0°$.

The opposite is occurring in the 2D LA regime (figure 9b). The wave profiles of these cases were shown earlier (figure 6) to be influenced more strongly by gravity, which results in steeper crests than troughs. Profile asymmetry of this type causes the wave-induced velocity under the crest to be higher than under the trough. This difference occurs throughout the liquid layer (because it is a relatively shallow layer), which leads to large deviations from the entire linear theory profile. Therefore, linear wave theory is unable to predict the wave-induced velocities measured in the 2D LA cases.

The mean radial velocities for the same cases as in figure 8 are shown in figure 10. In graph b), the cases from the 2D LA region have a negative (downward) radial velocity in the whole liquid layer. This is expected, since it was shown (e.g. Liné et al., 1996; Nordsveen, 2001) that the wave amplitude distribution in the spanwise direction in this wave regime (higher at the walls than in the centre) produces a secondary flow directed away from the interface in the centre of the pipe. In the 3D SA region, the wave pattern is more complex with waves having also substantial amplitudes in the centre. This occurs typically at higher gas velocities and results in cases **103**, **122** and **123** having a positive radial velocity, with a flow from the wall towards the interface. The difference in magnitudes of secondary flow between the two wave patterns is likely caused by the corresponding difference in wave heights (see figure 4), since the nonuniform wave amplitude distribution (and not the turbulence anisotropy) is the main cause of secondary flows in the liquid at the present conditions.

The velocity data extracted from the instantaneous velocity fields are processed to determine the Reynolds normal stresses (for the axial and radial direction) and the Reynolds shear stresses. The Reynolds stresses are scaled with u_τ and presented in figures 11 and 12. In the 3D SA regime (figure 11a), the Reynolds stress profiles are the result of both the turbulence near the wall and the wave motion near the interface. The turbulence in the near-wall shear layer produces a peak in the axial stress profile of $\sim$2.7 at $y^+ \sim 15$; this was also observed previously by Eggels et al. (1994) in single-phase turbulent pipe flow. However, close to the interface (at $y^+ > 50$), the wave-induced fluctuations produce an increase in stress levels, and this is particularly pronounced in cases with higher wave heights (**103**, **122** and **123**). In the 2D LA regime (figure 11b), a different behaviour is observed. It appears that wave-induced motion is so intense that it affects

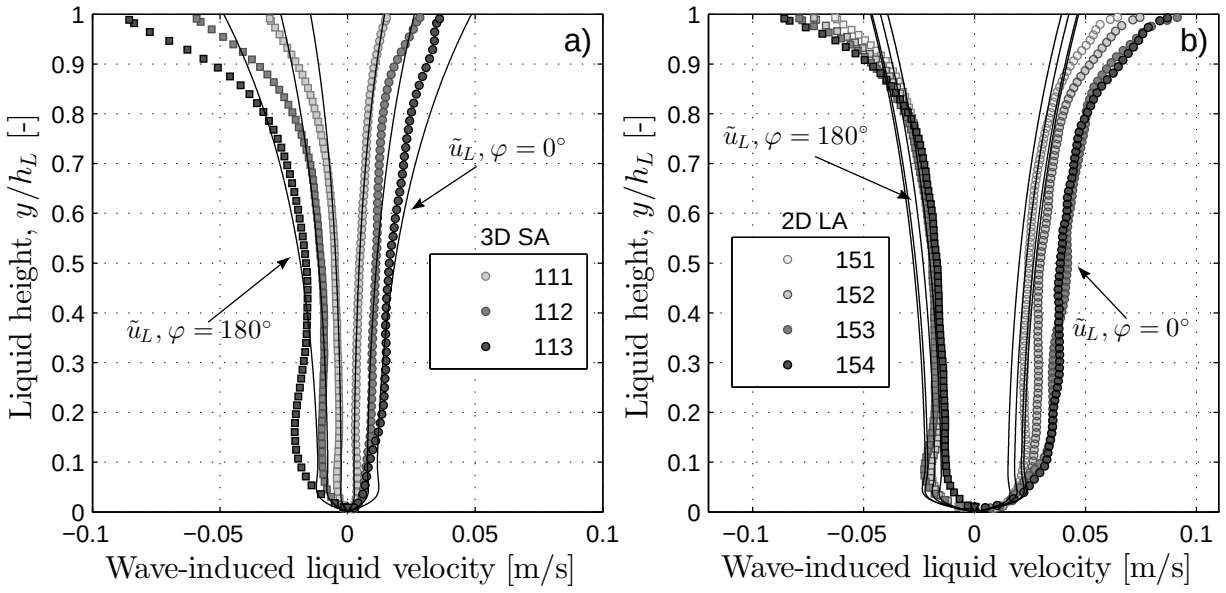

Figure 9: Measured wave-induced axial $\tilde{u}_L$ and radial $\tilde{v}_L$ liquid velocity profiles for cases along lines a) L2 (3D SA regime) and b) L6 (2D LA regime), at the crest ($\varphi = 0°$) and the trough ($\varphi = 180°$) of the wave. Axial velocity at the crest is indicated with circles and at the trough with squares. Radial velocity at the crest is indicated with upward pointing triangles and at the trough with downward pointing triangles. Solid lines are velocities predicted by linear wave theory.

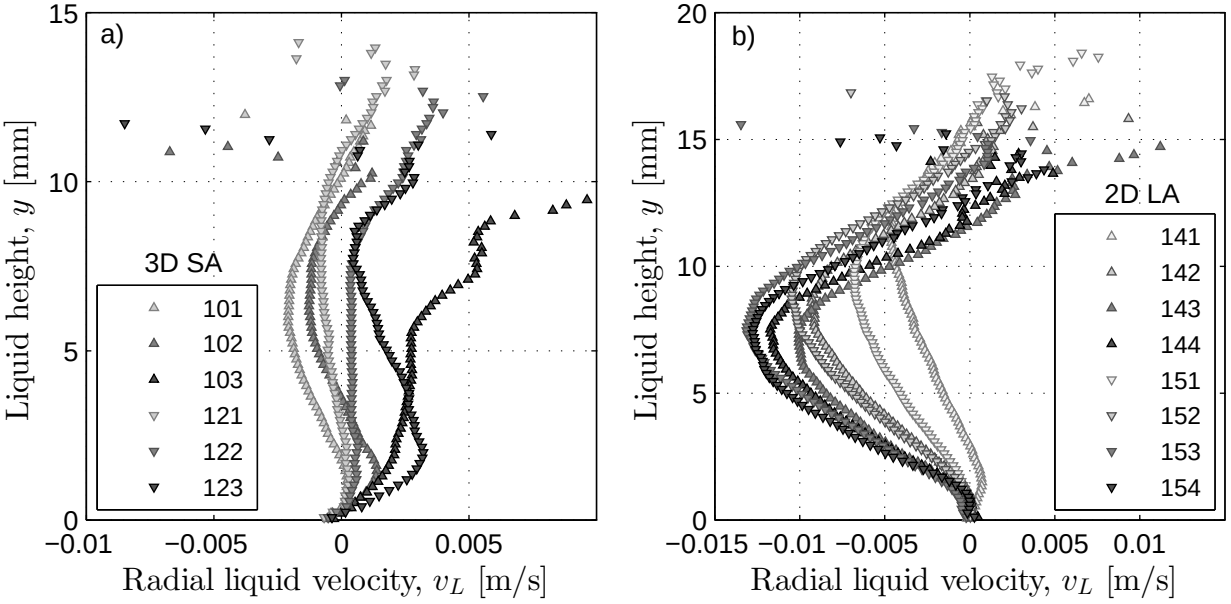

Figure 10: Measured mean radial liquid velocity profiles for cases along lines a) L1 and L3 (3D SA regime) and b) L5 and L6 (2D LA regime).

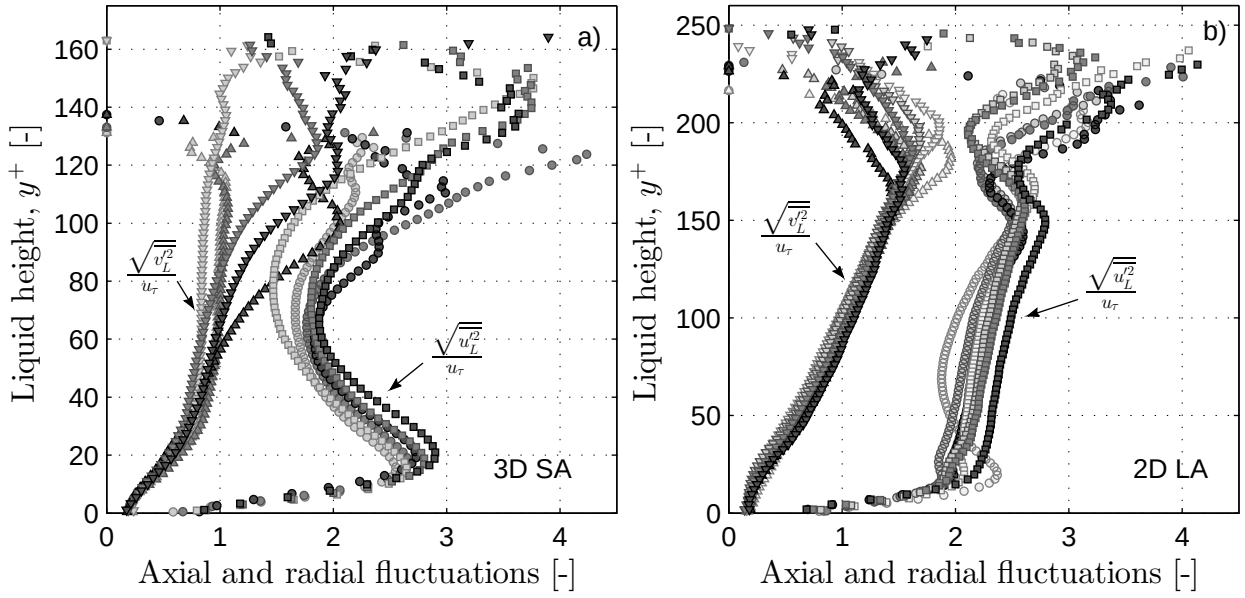

Figure 11: Measured liquid axial and radial Reynolds stress profiles for cases along lines a) L1 and L3 (3D SA regime) and b) L5 and L6 (2D LA regime), scaled with the measured friction velocity u_τ. The symbols correspond to those of figures 8 and 10

the Reynolds stresses in the entire liquid layer. Both the axial and the radial Reynolds stress profiles show a gradual increase towards the interface, mirroring the shape of the wave-induced velocity in these conditions (see figure 9). Interestingly, the axial stress profile of case **141** appears to be somewhere in between the profiles of the two wave patterns. This is because the waves for case **141** are not as high as in the other cases in the 2D LA regime. Therefore, the influence of the near-wall turbulence can still be detected.

Finally, figure 12 shows the Reynolds shear stresses for the same cases. Here also, the effects of turbulence and waves are combined to arrive at the final stress profiles. In cases **101** and **102**, where the waves are relatively low, the Reynolds shear stress profile resembles a typical shear-layer profile with a maximum of approx. 0.7 at $y^+ \sim 30$ (see e.g. Eggels et al., 1994) that reduces gradually in the bulk of the flow. As the waves become higher and longer (e.g. when moving through the 3D SA wave regime towards the 2D LA wave regime) the values in the bulk become lower; the near-wall peak becomes much smaller than in single-phase shear-layers, and the profile in the bulk attains negative values. This is explained by the addition of the wave-induced fluctuations to the turbulence-induced fluctuations already present in the smooth flow (see e.g. Birvalski et al., 2014). The waves induce a velocity pattern which contains fluctuations that are either negative, positive or zero, depending on the wave phase. For example, if the wave crest is phase 0°, the trough phase 180° and the windward zero-crossing phase 90°, the velocity fluctuations between phases 0° and 90° would be positive, as well as those between 180° and 270°. Similarly, velocity fluctuations between 90° and 180° and those between 270° and 0° (−90° and 0°) would be negative. In sinusoidal waves, it is expected that the sum of these fluctuations amounts to zero. In the real wave field measured in our experiments, however, in which the waves are asymmetrical in all directions, the sum amounts to a negative value.

A behaviour similar to that presented in figures 8-12 has been reported previously by Fabre et al. (1987) and Fernandino & Ytrehus (2008) in channels. Although the stratified flow in pipes is somewhat more complex since the flow depth changes in the spanwise direction (which, consequently, influences the wave height distribution in that direction), the present study shows that the general trends of the mean and the fluctuating liquid flow profiles are the same for both channels and pipes.

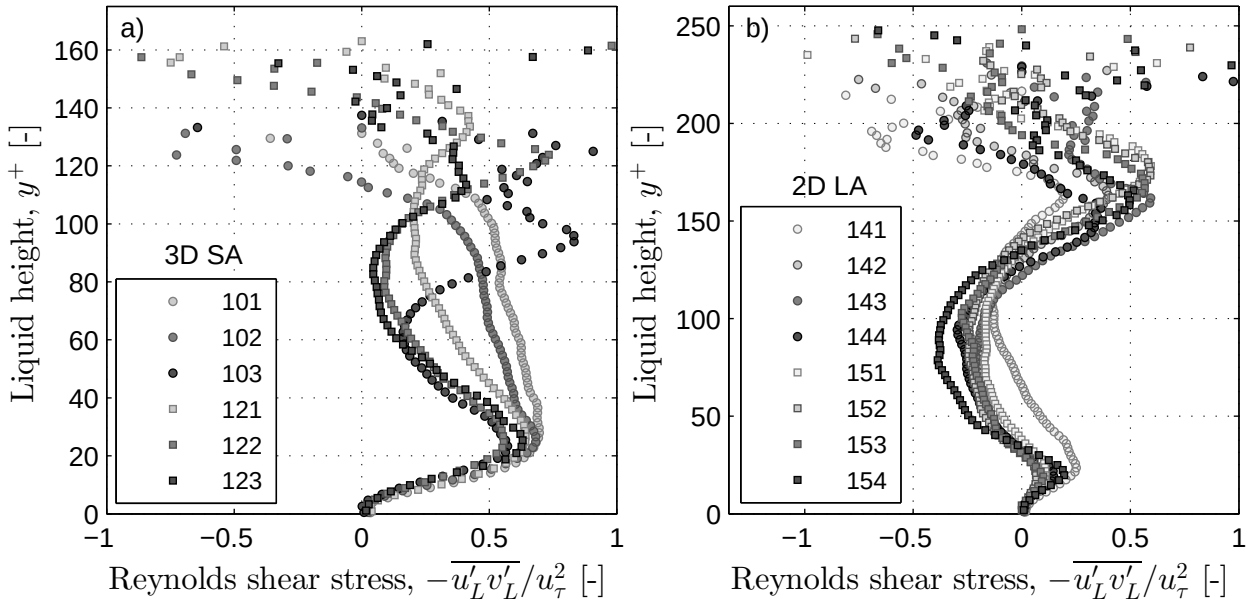

Figure 12: Measured liquid Reynolds shear stress profiles for cases along lines a) L1 and L3 (3D SA regime) and b) L5 and L6 (2D LA regime), scaled with the measured friction velocity u_τ.

4.4. Gas velocities

Time-averaged quantities in the air phase were derived by extracting instantaneous velocity profiles at three axial locations (equally spaced within the FOV) and averaging them in an Eulerian coordinate system. As mentioned in Section 3, the origin of the coordinate system is fixed at the top pipe wall. The x-coordinate points downstream and the y-coordinate points towards the pipe centre.

The time-averaged gas velocity is presented in figure 13. In graph a), velocity and height are scaled using the gas friction velocity $u_{\tau G}$, which was obtained from the classical Blasius relation for the friction factor $f_B = 0.3164 \mathrm{Re_G}^{-0.25}$, where $\mathrm{Re_G} = u_G D_{Gh}/\nu_G$ and D_{Gh} is the hydraulic diameter for the gas phase. The friction velocity could not be obtained directly from the u_G profile, because the results contained typically only one measurement point in the viscous sublayer ($y^+ < 5$, where for the gas phase $y^+ = \frac{y u_{\tau G}}{\nu_G}$). However, the resulting $u_{\tau G}$ values were found to be consistent with the values of $u_{\tau G}$ found from the measured Reynolds shear stress profiles (see later, figure 14). This was done by extrapolating a straight line fitted to the linear part of the total shear stress profile up to the wall, and taking the square root of the value at the wall. The values of $u_{\tau G}$ determined with the two methods differ by less than 3%. In figure 13, the log-law with κ=0.4 and B=5.5 is also shown. The agreement between the mean velocity profiles (which include both wave regimes) and the log-law is seen to be very good. This means that the boundary layer at the top wall does not differ substantially from a single-phase flow boundary layer, i.e. the effects of the waves do not reach the top pipe wall. Similar observations have been reported by Andreussi & Persen (1987) and Paras et al. (1998).

Mean axial gas velocity profiles scaled by the maximum velocity are shown in figure 13b for cases belonging to lines L2 and L5. The radial coordinate is scaled by the gas phase height $D-h_L$. Velocity profiles approximately form three groups. The first group (made up of cases **111**, **112** and **141** with a relatively small wave height) has rather symmetrical profiles, with the highest velocities reached at $y/(D-h_L) \cong 0.5$. The second group (consisting of case **113**) has relatively high gravity-capillary waves, and its profile is asymmetric. It shows a 'belly' on the side closer to the interface, with the maximum velocity point displaced slightly downwards. The third group (made up of cases **142-144** with gravity waves) is also asymmetrical, but the location of the maximum velocity is displaced upwards to $y/(D-h_L) \cong 0.45$.

A similar asymmetry in the mean velocity profiles and displacement of the maximum velocity point

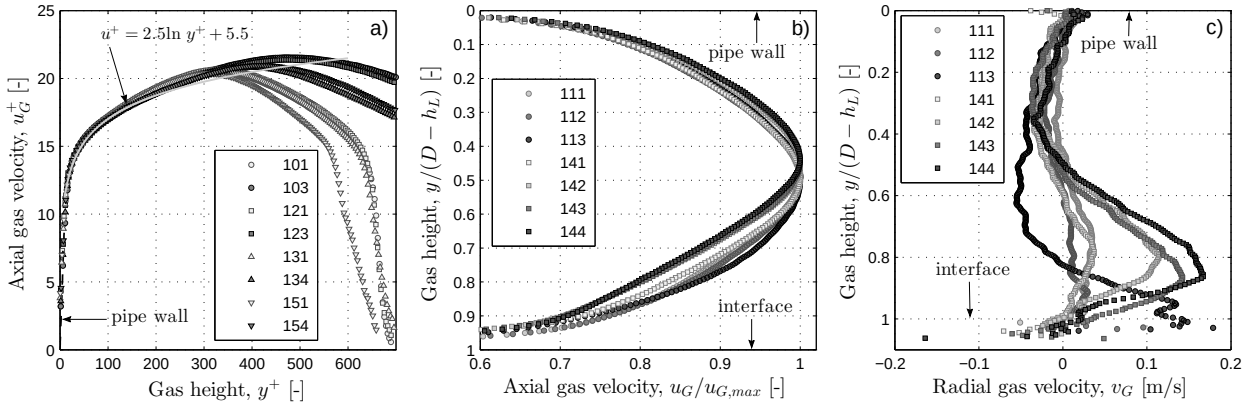

Figure 13: Measured mean axial gas velocity profiles for cases along lines L1, L3, L4 and L6 (a), scaled with the friction velocity $u_\tau G$, and L2 and L5 (b), scaled with the maximum profile velocity $u_{G,max}$. The law of the wall with $\kappa = 0.4$ and $B = 5.5$ is shown for comparison in graph a). Measured mean radial gas velocity profiles for cases along lines L2 and L5 are shown in graph c). The radial coordinate is scaled with the gas phase height $(D - h_L)$.

in two-phase flows has been reported by e.g. Fabre et al. (1987), Dykhno et al. (1994) and Paras et al. (1998) and was interpreted as a consequence of secondary flows. These secondary flows are caused by the turbulence anisotropy in the cross-section (Liné et al., 1996) due to either an asymmetric flow geometry (flow in non-circular ducts) or due to an asymmetric distribution of wall roughness. The overall effect of anisotropy is the formation of secondary flow patterns directed towards the sources of anisotropy (corners, or places with high wall roughness). In two-phase pipe flows, both sources of turbulence anisotropy are present: the gas phase experiences an asymmetric flow geometry and the waves act like a wall roughness that is higher than that of the smooth pipe wall. Secondary flows for cases studied previously are presented in figure 13c. The profiles of the mean radial velocity v_G again appear to form three groups corresponding to the groups observed in the previous figure. The cases with smaller waves (**111**, **112** and **141**) have a relatively weak secondary flow directed downwards in the top half of the pipe and upwards in the bottom part. This suggests the existence of four flow cells in the pipe cross-section. In the middle of the gas space, where they all meet, the flow is oriented along three directions: 1) vertical, where the fluid is moving towards the centre, away from the interface and the top wall (seen in figure 13c), and 2-3) along the two lines connecting the centre with the corners, where the fluid is moving away from the centre, towards the corners. This secondary flow pattern appears to be caused predominantly by the asymmetric flow geometry, since similar v_G profiles were detected also in turbulent non-wavy flow. Several cases were measured that covered the transition to turbulence in the gas phase (with a laminar liquid phase). These had a smooth interface, and the onset of secondary flow as the gas was becoming turbulent was clearly visible (not shown).

The second and the third group of cases (composed of **113** and **142-144**, respectively) has a strong upward and downward directed flow in the bulk of the gas phase, respectively, which corresponds to the displacement of the maximum axial velocity point, shown in figure 13. Close to the top wall, however, these cases appear not to be influenced by the secondary flows caused by, in these conditions, the highly asymmetric wall roughness as a consequence of waves. Case **113** has a predominantly downward directed flow, as is expected when the waves have substantial amplitudes also in the pipe centre. This complements the upward directed flow in the liquid phase measured in cases with the same u_{SG} (**103** and **123**, figure 10). However, the explanation of the profile shape for this case appears to be even more complex, because there is also a small region with positive velocity close to the interface. Finally, the gravity wave cases (**142-144**) have a strong upward directed v_G (which was measured also in channels (Fabre et al., 1987)) that is due to turbulence anisotropy caused by the varying wave amplitude in the spanwise direction (Liné et al., 1996). A complementary downward directed v_L profile was shown in figure 10.

The Reynolds stress profiles for the same cases are presented in figure 14. The axial, radial and shear stresses are scaled by the gas friction velocity $u_{\tau G}$ and the radial coordinate is scaled with the gas phase

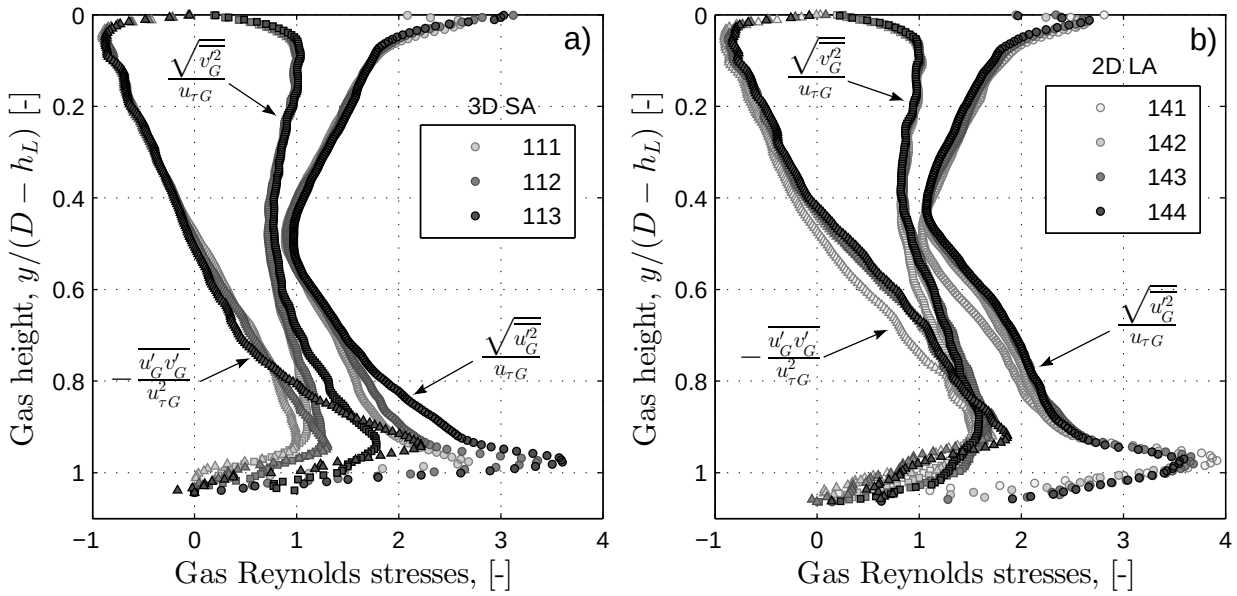

Figure 14: Measured axial (circles), radial (squares) and shear (triangles) Reynolds stress profiles for cases along lines L2 (a) and L5 (b), scaled with the friction velocity $u_\tau G$. The radial coordinate is scaled with the gas phase height $(D - h_L)$.

height D-h_L. As expected, in the top half of the gas height, both the 3D SA and the 2D LA cases have Reynolds stress profiles which correspond well with those of single-phase pipe flow (see e.g. den Toonder & Nieuwstadt, 1997). However, large deviations are seen in the bottom half, with all the fluctuations reaching higher levels as the wave height increases. The vertical extension of these deviations also increases with H, from a scaled gas height of about 0.1-0.3 in 3D SA cases to about 0.5-0.6 in 2D LA cases. Finally, it is observed that the position of zero Reynolds shear stress moves slightly downward with increasing u_{SG} in the L2 cases, and upward in the L5 cases. This position coincides with the position of maximum axial velocity (see figure 13) in all the measurements.

5. Conclusions

Experiments were performed in stratified wavy two-phase flow of air and water in a 5 cm diameter horizontal pipe. The objective of the present study was to investigate the transition from the 3D small amplitude (3D SA) to the 2D large amplitude (2D LA) wave pattern by measuring the interfacial statistics and the velocities in both phases.

The wave characteristics obtained from profile camera images showed that the 3D SA wave pattern consisted of a relatively short wavelength (approx. 25-30 mm) and low amplitude (less than 2 mm) waves, with a steepness that changes substantially with gas velocity (figure 4). The 2D LA waves, on the other hand, were longer (approx. $50-60$ mm) and higher (greater than 2 mm) and grew in height and length with increasing liquid velocity, keeping the wave steepness approximately constant. Due to their length, both wave patterns belonged to the gravity-branch of the dispersion relation (as given by linear wave theory). The shorter 3D SA wave pattern could be classified as gravity-capillary waves and the longer 2D LA pattern as gravity waves. The effect of the two restoring forces (capillarity and gravity) could also be seen in the profile shapes. Namely, there was a trend of reduction of the influence of the capillary force when moving from the 3D SA to the 2D LA region, with the profile shape attaining a steeper and higher crest due to the increasing effect of gravity. The boundary between the two wave patterns was determined visually. It consisted of a wide region in which waves have characteristics typical of both wave patterns. This was shown

in figure 7, where an emergence of one wave type was observed to coincide with the gradual disappearance of the other, with the wave frequency approximately halving during this process.

Further differences between the 3D SA and the 2D LA wave regimes, caused by the different wave properties, were observed in the time- and phase-averaged liquid velocities. Overall, the 2D LA wave pattern - as opposed to the 3D SA pattern - was shown to modify the velocities in the whole shear layer, with the exception of a thin near-wall region ($y^+ < 30$). This is best seen in profiles of time-averaged axial velocity and the Reynolds stresses (figures 8, 11 and 12).

The velocities measured in the gas phase - in contrast to the wave properties and the liquid velocities - did not show a substantial difference between the two wave patterns. The only exception was the shape of the gas velocity profile (figure 13), which was slightly skewed depending on the secondary flow. The secondary flow in turn depends on the wave height distribution in the spanwise direction, which is different for the two wave patterns (figure 3). Apart from this, the waves displayed the same effect in all the cases: they enhanced the turbulent fluctuations in the near-interface region, with fluctuations becoming higher with increasing H and H/λ (figure 14).

Acknowledgments

The support of Shell Projects & Technology in financing this study is gratefully acknowledged.

References

Andreussi, P., & Persen, L. N. (1987). Stratified gas-liquid flow in downwardly inclined pipes. *Int. J. Multiphase Flow*, *13(4)*, 565–575.

Andritsos, N., & Hanratty, T. J. (1987). Interfacial instabilities for horizontal gas-liquid flows in pipelines. *Int. J. Multiphase Flow*, *13(5)*, 583–603.

Ayati, A., Kolaas, J., Jensen, A., & Johnson, G. (2015). Combined simultaneous two-phase piv and interface elevation measurements in stratified gas/liquid pipe flow. *Int. J. Multiphase Flow*, *74*, 45–58.

Ayati, A. A., Kolaas, J., Jensen, A., & Johnson, G. W. (2014). A PIV investigation of stratified gas-liquid flow in a horizontal pipe. *Int. J. Multiphase Flow*, *61*, 129–143.

Birvalski, M. (2015). *Experiments in stratified gas-liquid pipe flow*. Ph.D. thesis Delft University of Technology, Delft, The Netherlands.

Birvalski, M., Tummers, M. J., Delfos, R., & Henkes, R. A. W. M. (2014). PIV measurements of waves and turbulence in stratified horizontal two-phase pipe flow. *Int. J. Multiphase Flow*, *62*, 161–173.

Birvalski, M., Tummers, M. J., Delfos, R., & Henkes, R. A. W. M. (2015). Laminar-turbulent transition and wave-turbulence interaction in stratified horizontal two-phase pipe flow. *J. Fluid Mech.*, *780*, 439–456.

Bontozoglou, V., & Hanratty, T. J. (1990). Capillary-gravity kelvin-helmholtz waves close to resonance. *J. Fluid Mech.*, *217*, 71–91.

Dean, R. G., & Dalrymple, R. A. (1998). *Water wave mechanics for engineers and scientists*. World Scientific Publishing Co. Pte. Ltd.

Dykhno, L. A., Williams, L. R., & Hanratty, T. J. (1994). Maps of mean gas velocity for stratified flows with and without atomization. *Int. J. Multiphase Flow*, *20(4)*, 691–702.

Eggels, J. G. M., Unger, F., Weiss, M. H., Westerweel, J., Adrian, R. J., Friedrich, R., & Nieuwstadt, F. T. M. (1994). Fully developed turbulent pipe flow: a comparison between direct numerical simulation and experiment. *J. Fluid. Mech.*, *268*, 175–209.

Espedal, M. (1998). *An experimental investigation of stratified two-phase pipe flow at small inclinations*. Ph.D. thesis Norwegian University of Science and Technology, Trondheim, Norway.

Fabre, J., Masbernat, L., & Suzanne, C. (1987). Stratified flow, part i: local structure. *Multiphase Sc. and Technol.*, *3*, 285–301.

Fernandino, M., & Ytrehus, T. (2006). Determination of flow sub-regimes in stratified air-water channel flow using LDV spectra. *Int. J. Multiphase Flow*, *32(4)*, 436–446.

Fernandino, M., & Ytrehus, T. (2008). Effect of interfacial waves on turbulence structure in stratified duct flows. *J. Fluid Eng.-T. ASME*, *130*, 061201(1–8).

Flores, A. G., Crowe, K. E., & Griffith, P. (1995). Gas-phase secondary flow in horizontal, stratified and annular two-phase flow. *Int. J. Multiphase Flow*, *21(2)*, 207–221.

Hussain, A. K. M. F., & Reynolds, W. C. (1970). The mechanics of an organized wave in turbulent shear flow. *J. Fluid Mech.*, *41(2)*, 241–258.

Janssen, P. A. E. M. (1986). The period-doubling of gravity-capillary waves. *J. Fluid. Mech.*, *172*, 531–546.

Liné, A., Masbernat, L., & Soulamia, A. (1996). Interfacial interactions and secondary flows in stratified two-phase flow. *Chem. Eng. Comm.*, *141–142*, 303–329.

Mukto, M. A., Atmane, M. A., & Loewen, M. R. (2007). A particle-image based wave profile measurement technique. *Exp. Fluids*, *42*, 131–142.

Nordsveen, M. (2001). Wave- and turbulence-induced secondary currents in the liquid phase in stratified duct flow. *Int. J. Multiphase Flow*, *27*, 1555–1577.

Paras, S. V., & Karabelas, A. J. (1992). Measurements of local velocities inside thin liquid films in horizontal two-phase flow. *Exp. Fluids*, *13*, 190–198.

Paras, S. V., Vlachos, N. A., & Karabelas, A. J. (1998). LDA measurements of local velocities inside the gas phase in horizontal stratified/atomization two-phase flow. *Int. J. Multiphase Flow*, *24(4)*, 651–661.

Reichardt, H. (1951). Vollständige darstellung der turbulenten geschwindigkeitsverteilung in glatten leitungen. *Zeitschrift für Angewandte Mathematik und Mechanik*, *31(7)*, 208–219.

Sanchis, A., Johnson, G. W., & Jensen, A. (2011). The formation of hydodynamic slugs by the interaction of waves in gas-liquid two-phase flow. *Int. J. Multiphase Flow*, *37*, 358–368.

Siddiqui, M. H. K., & Loewen, M. R. (2007). Characteristics of the wind drift layer and microscale breaking waves. *J. Fluid Mech.*, *573*, 417–456.

Siddiqui, M. H. K., & Loewen, M. R. (2010). Phase-averaged flow properties beneath microscale breaking waves. *Boundary-Layer Meteorol.*, *134*, 499–523.

Strand, O. (1993). *An experimental investigation of stratified two-phase flow in horizontal pipes*. Ph.D. thesis University of Oslo, Oslo, Norway.

den Toonder, J. M. J., & Nieuwstadt, F. T. M. (1997). Reynolds number effects in a turbulent pipe flow for low to moderate re. *Phys. Fluids*, *9*, 3398–3409.

Vestøl, S., & Melaaen, M. (2007). PIV and gamma measurements of stratified unprocessed gas flow in a horizontal and near horizontal test pipe. In *Proc.* 13^{th} *Int. Conf. on Multiphase Prod. Technol.* (pp. 237–250).